Research Article Vol. 9, No. 4 / April 2021 / Photonics Research 615

PHOTONICS Research

Characterization of field-effect mobility at optical frequency by microring resonators

Wei-Che Hsu, Erwen Li, Bokun Zhou, and Alan X. Wang*

School of Electrical Engineering and Computer Science, Oregon State University, Corvallis, Oregon 97331, USA
*Corresponding author: wang@oregonstate.edu

Received 4 December 2020; revised 2 February 2021; accepted 14 February 2021; posted 16 February 2021 (Doc. ID 416656); published 31 March 2021

A novel characterization method is proposed to extract the optical frequency field-effect mobility ($\mu_{op,FE}$) of transparent conductive oxide (TCO) materials by a tunable silicon microring resonator with a heterogeneously integrated titanium-doped indium oxide (ITiO)/SiO_2/silicon metal–oxide–semiconductor (MOS) capacitor. By operating the microring in the accumulation mode, the quality factor and resonance wavelength shift are measured and subsequently used to derive the $\mu_{op,FE}$ in the ultra-thin accumulation layer. Experimental results demonstrate that the $\mu_{op,FE}$ of ITiO increases from 25.3 to 38.4 $cm^2 \cdot V^{-1} \cdot s^{-1}$ with increasing gate voltages, which shows a similar trend as that at the electric frequency.

https://doi.org/10.1364/PRJ.416656

1. INTRODUCTION

Metal–oxide–semiconductor (MOS) capacitors are one of the most prevailing electronic device structures, and have laid the foundation of modern transistors that have transformed the entire industry of microelectronics [1]. In recent years, MOS devices have also gained increasing utility in photonic applications, which could pave the way for a new generation of hybrid electronic–photonic systems [2,3]. MOS-driven silicon photonic devices in particular have rapidly become one of the most promising building blocks for future optical interconnect systems due to their enhanced performance in electro-optic (E-O) modulation and scalability of fabrication [4–6]. Photonic devices based on the MOS structure usually operate in the accumulation mode. When a negative bias voltage (V_g) is applied, it induces the field effect and modifies the refractive indices of the semiconductor materials through the plasma dispersion effect so that an optical phase shift is induced to the guided light. In addition to their intrinsic advantages, MOS structures provide feasibility of heterogeneous integration with other materials such as graphene, III-V, and transparent conductive oxides (TCOs) on silicon photonics [7–9]. Of these heterogeneously integrated photonic devices, an MOS device with a TCO gate can achieve unity-order refractive index changes in the accumulation layer [10]. Several ultra-efficient Si-TCO photonic devices have been reported using a Mach–Zehnder interferometer, an electro-absorption modulator, a photonic crystal nanocavity, and a microring resonator (MRR) [9,11–13].

Carrier mobility is one of the most pivotal properties of semiconductors, as it can determine the performance of solid-state devices. Carrier mobility represents the velocity of electrons or holes under certain electric fields, and therefore it determines the conductivity and frequency response of electronic devices such as transistors. Thus, the high mobility of semiconductors is critical to achieving high bandwidth and low power dissipation [14]. For photonic devices, the impact of carrier mobility reaches even further. As described by the Drude model, the collision frequency [Eq. (1c)], which is the collision process between free carriers and ionized impurities in TCOs, is inversely proportional to the carrier mobility at the optical frequency [15,16]. Furthermore, the optical loss due to free carrier absorption is determined by the imaginary part of the complex permittivity [Eq. (1a)], which is influenced by the collision frequency as well. Hence, high-mobility semiconductors are critical to low optical loss waveguides. For instance, previous research has shown that high-mobility TCOs can significantly enhance the performance of photonic modulators by increasing the extinction ratio, improving the energy efficiency and quality factor (Q factor) [13,17,18].

The carrier mobility of semiconductors at electrical frequency (DC or RF) is usually measured by the Hall effect. It actually measures the bulk mobility (μ_{bulk}), which is the average mobility of the entire thin film layer [19,20]. For many electronic devices, field-effect mobility (μ_{FE}) is even more critical to determining the device performance. When a bias V_g is applied to the gate, the field effect induces accumulation or inversion layer at the surface of the semiconductor with the insulator, forming a channel of free charges that are drastically different than those in the bulk materials [10,21]. The carrier mobility in the accumulation or inversion layer, which is also

called the field-effect mobility μ_{FE}, is generally higher than μ_{bulk} because the high concentration of free carriers in the channel layer brings an electrostatic screening effect that reduces impurity coulomb scattering [22]. This phenomenon has been verified by thin-film transistors (TFTs) [23], and TFTs have been used to measure the electric frequency μ_{FE}. The measurements of the gate voltage, drain voltage, and drain current are used to extract the electric frequency μ_{FE}. For example, experimental results show that the electric frequency μ_{FE} of TCOs increases as the V_g increases [24–28].

In contrast to electric frequency mobility, which is limited by ionized-impurity scattering and grain-boundary scattering, the optical frequency mobility (μ_{op}) is insensitive to grain-boundary scattering. It is only determined by ionized-impurity scattering because the average electron path length, which is in the range of a few nanometers and under the application of a rapidly oscillating electric field, is much smaller than the grain size [29]. By comparing the difference between electrical and optical frequency carrier mobility, we can observe the contribution from the grain-boundary scattering and ionized-impurity scattering separately [30]. The optical frequency bulk mobility ($\mu_{op,bulk}$) of a semiconductor film on a thick substrate is usually characterized by a spectroscopic ellipsometry [31]. However, ellipsometry cannot effectively measure the optical frequency field-effect mobility ($\mu_{op,FE}$) due to the ultrathin accumulation layer (~1 nm). The accumulation layer is only around 0.1% of the probing wavelength used in the ellipsometry, which cannot induce meaningful light–matter interaction to calculate the film's refractive index and thickness. Therefore, a fundamentally different method is needed for the measurement of $\mu_{op,FE}$ in the ultra-thin accumulation layer.

In this paper, we propose a novel characterization method to extract the $\mu_{op,FE}$ of TCO materials using an MRR on a silicon-on-insulator (SOI) wafer. This method works for all TCOs and can even be applied to other types of semiconductor materials. In this paper, titanium-doped indium oxide (ITiO) is used in the experiment for $\mu_{op,FE}$ characterization due to its potential for high mobility. An ITiO-SiO_2-Si MOS-driven MRR is fabricated through heterogeneous integration, which can provide orders of magnitude stronger light–matter interaction compared with ellipsometry measurement. By operating the MRR in the accumulation mode with negative V_g, the Q factors and resonance wavelength shift ($\Delta\lambda$) values are measured and subsequently used to derive the $\mu_{op,FE}$ in the ultra-thin accumulation channel. Experimental results in this work demonstrate that the $\mu_{op,FE}$ of ITiO increases from 25.3 to 38.4 $cm^2 \cdot V^{-1} \cdot s^{-1}$ with increasing negative V_g. This proposed $\mu_{op,FE}$ measurement technique will provide an effective characterization method for field-effect electro-optic devices, especially for heterogeneously integrated silicon photonic devices.

2. DESIGN AND PRINCIPLE

A. Design of ITiO-gated MOS MRR

To derive the $\mu_{op,FE}$ of ITiO in the accumulation layer, an SOI waveguide MRR is driven by a hybrid ITiO-SiO_2-Si MOS capacitor operating in the accumulation mode. Figure 1(a) shows the three-dimensional (3D) schematic of the ITiO-gated MOS MRR. The active region consists of a p-type Si (p-Si) waveguide, a silicon dioxide (SiO_2) insulation layer, and an ITiO gate. The p-Si waveguide, which is based on a 400 nm × 250 nm rib waveguide with a 50 nm partially etched slab, also

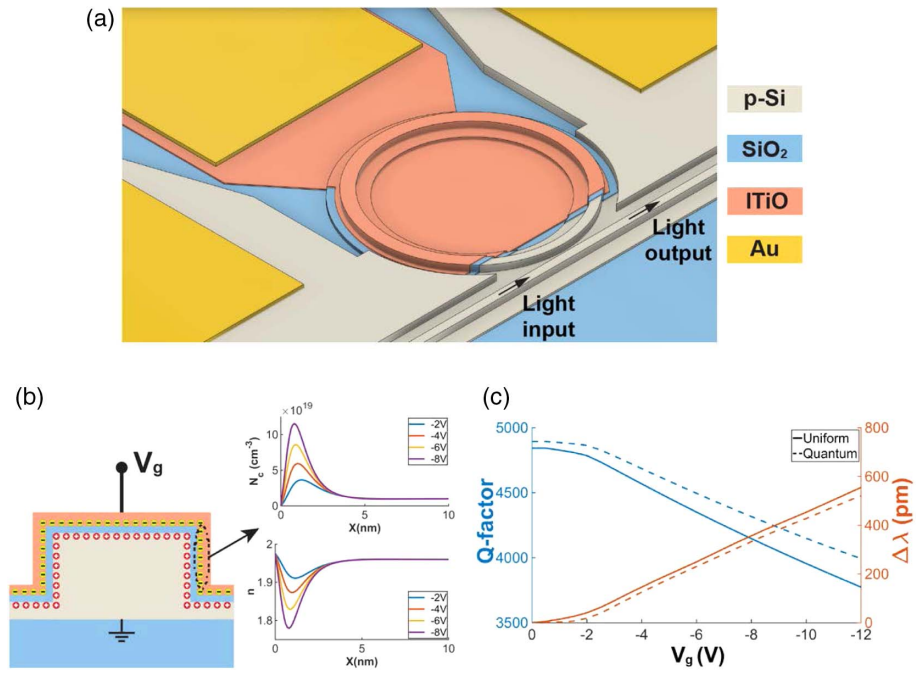

Fig. 1. (a) 3D schematic of ITiO-Si-SiO_2 MOS-driven MRR. (b) Cross-sectional schematic in the active region. With the negative V_g, it induces the carrier accumulation and refractive index modulation in the ITiO and Si layers. (c) Simulated results with different models: quantum-moment model plots in dashed lines and uniform model plots in solid lines. Q factor (blue line, left y axis) and resonance wavelength shift $\Delta\lambda$ (red line, right y axis) as a function of V_g.

serves as the bottom substrate of the MOS capacitor with the connection to the ground metal electrodes. The SiO_2 covers the p-Si MRR as the oxide layer and the ITiO layer acts as the top gate, which is connected to the gate electrode. The optical properties of TCO materials can be described by the Drude model [32]:

$$\varepsilon(\omega) = \varepsilon_\infty - \frac{\omega_p^2}{\omega^2+\gamma^2} + i\frac{\omega_p^2\gamma}{(\omega^2+\gamma^2)\omega}, \tag{1a}$$

where ε_∞ is the high-frequency dielectric constant of the material.

The plasma frequency (ω_p) is related to the carrier concentration (N_c) by

$$\omega_p = \frac{N_c e^2}{\varepsilon_0 m^*}, \tag{1b}$$

where e is the electron charge, ε_0 is the vacuum permittivity, and m^* is the effective mass of charge carriers.

The plasma collision frequency (γ) is related to the μ_{op} by

$$\gamma = \frac{e}{m^*\mu_{op}}. \tag{1c}$$

The cross-sectional schematic in the active region of the device is shown in Fig. 1(b). Applying a negative V_g on the ITiO gate induces electron accumulation at the ITiO/SiO_2 interface and hole accumulation at the p-Si/SiO_2 interface. This field effect changes the optical permittivities of ITiO and Si, which influences the resonance wavelengths (λ_{res}) and Q factors of the silicon MRR. The Q factor can be written as [33]

$$Q = \frac{\pi n_g L\sqrt{ra}}{\lambda_{res}(1-ra)}, \tag{2a}$$

where r is the self-coupling coefficient, a is the single-pass amplitude transmission, L is the circumference of a ring, and n_g is the group index of the ring waveguide.

The value of a is related to the loss α by

$$a^2 = e^{-\alpha L}. \tag{2b}$$

The values of r and a are crucial to the Q factor. r is determined by the coupling between the bus waveguide and microring and can be adjusted by changing the waveguide gap or coupling length [34,35]. a is affected by the loss from the accumulation layers of ITiO and p-Si when the negative V_g is applied. Hence, applying a moderate V_g changes a while not affecting r. At the critical coupling ($r = a$) condition, the transmission at λ_{res} decreases to zero [33,36]. When the loss of the MRR is fixed, the Q factor can be improved by working at the critical coupling condition [37].

The $\Delta\lambda$ can be calculated by the change of the effective index (n_{eff}):

$$\Delta\lambda = -\frac{\Delta n_{eff}}{n_{eff}}\lambda_{res}. \tag{3a}$$

As shown in Fig. 1(a), the ITiO does not cover the whole ring. Therefore, the n_{eff} depends on the length of the microring covered by the ITiO electrode, which can be written as

$$n_{eff} = P \times n_{eff,active} + (1-P) \times n_{eff,coupling}, \tag{3b}$$

where $n_{eff,active}$ is the effective index in the active region covered by ITiO and the $n_{eff,coupling}$ is the effective index in the coupling region without the coverage of ITiO. P is the ITiO coverage percentage on the MRR.

To understand how the Q factor and $\Delta\lambda$ are affected by V_g, we simulated an ITiO-gated MOS MRR with a radius of 6 μm by the finite-difference-eigenmode (FDE) solver in Lumerical MODE software. The carrier concentration distribution is simulated by Silvaco and imported into Lumerical MODE. The simulation results are plotted with dashed lines in Fig. 1(c). When a negative V_g is applied, it increases the N_c, and changes the relative permittivity [Eqs. (1a) and (1b)] of ITiO, which will further modulate the effective index n_{eff} of the guided mode in the microring waveguide calculated by Lumerical. The reduction of the real part of n_{eff} blueshifts the resonance wavelength as given in Eq. (3a), while the increase of the imaginary part of the n_{eff} increases the optical loss and reduces the Q factor as explained in Eqs. (2a) and (2b). Figure 1(c) shows the downward trend of the Q factor and blueshift of $\Delta\lambda$ by applying the V_g.

B. Model Setup

In our previous work [38], we compared the free carrier distribution using the quantum-moment model and uniform model. The results showed that a significant difference only occurs at very large V_g that can turn TCOs into the ENZ condition. However, we are not characterizing $\mu_{op,FE}$ of TCO materials close to the ENZ condition in this paper. Approximating the numerical model by a uniform layer (ΔN) in the accumulation layer can greatly simplify the analysis without sacrificing the accuracy under a moderate V_g [38,39]. To quantify the influence of the uniform concentration, Fig. 1(c) shows the difference between the distribution and uniform concentration in the accumulation layer. Even at the maximum V_g of −12 V, it only induces 5% difference, which is comparable to other error sources. Therefore, we believe that the uniform accumulation layer approximation, as illustrated in Fig. 2(a), can provide acceptable accuracy. The FDE module simulates the optical field intensity ($|E|^2$) of the bending waveguide with an MOS structure, and the ITiO consists of the bulk layer and accumulation layer, as shown in Fig. 2(b). The N_c and the μ_{bulk} in the bulk layer are determined by the initial condition ($V_g = 0$ V). At the initial condition, there is no field effect on the ITiO, so the carrier concentration and mobility are identical in the bulk and accumulation layer ($\Delta N = 0$; $\mu_{op,FE} = \mu_{bulk}$). To achieve the highest Q factor, it assumes the initial condition is at critical coupling, so r equals a at $V_g = 0$ V.

When a negative V_g is applied, it induces the field effect and changes carrier concentration in the accumulation layer. We can sweep different ΔN to simulate different external V_g. We have already known that the electric frequency μ_{FE} increases under the field effect because an electrostatic screening effect reduces the ionized-impurities scattering when the concentration of accumulated free carriers increases [22]. As the $\mu_{op,FE}$ is also affected by ionized-impurities scattering, we expect that the $\mu_{op,FE}$ also changes under the field effect. Hence, we can sweep ΔN and $\mu_{op,FE}$ in the simulation, which will induce different α, n_g, and n_{eff} while running the FDE solver. α and n_g are used to calculate the Q factor with Eqs. (2a) and (2b), and the $\Delta\lambda$ can be obtained from

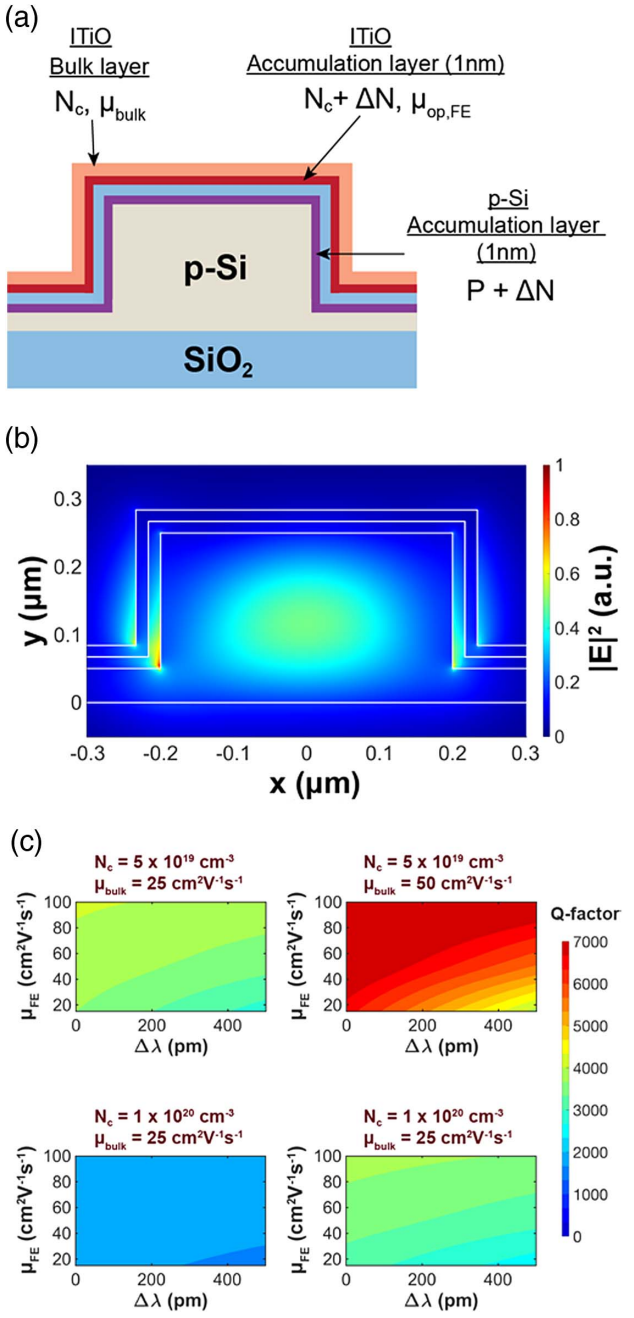

Fig. 2. (a) Simulation model includes the p-Si layer, SiO_2 layer, and the ITiO, consisting of the bulk material and 1 nm accumulation channel. (b) Simulated cross-sectional electric field intensity ($|E|^2$) distribution of the ITiO-gated MOS bending waveguide with a 17 nm SiO_2 layer and a 17 nm ITiO layer. (c) Q factor maps, with respect to $\mu_{op,FE}$ and $\Delta\lambda$, in different bulk conditions.

Eq. (3). After Q factors and $\Delta\lambda$ are obtained from the simulation, we can plot the Q factor map with respect to $\mu_{op,FE}$ and $\Delta\lambda$, as shown in Fig. 2(c). However, we can see that the Q factor maps are influenced by the initial conditions, i.e., N_c and μ_{bulk}. Therefore, the final Q factor map will be known when the initial condition is measured from the experiment. Finally, we can measure the experimental Q factor and $\Delta\lambda$ from the tunable MRR with negative V_g to derive the $\mu_{op,FE}$ by mapping the Q factor with the simulation results. Also, we can observe how the field effect changes the $\mu_{op,FE}$.

3. FABRICATION AND CHARACTERIZATION

A. Fabrication Processes and Testing

The ITiO-gated MRRs are fabricated on an SOI wafer. First, the bus waveguides, microrings, and grating couplers are

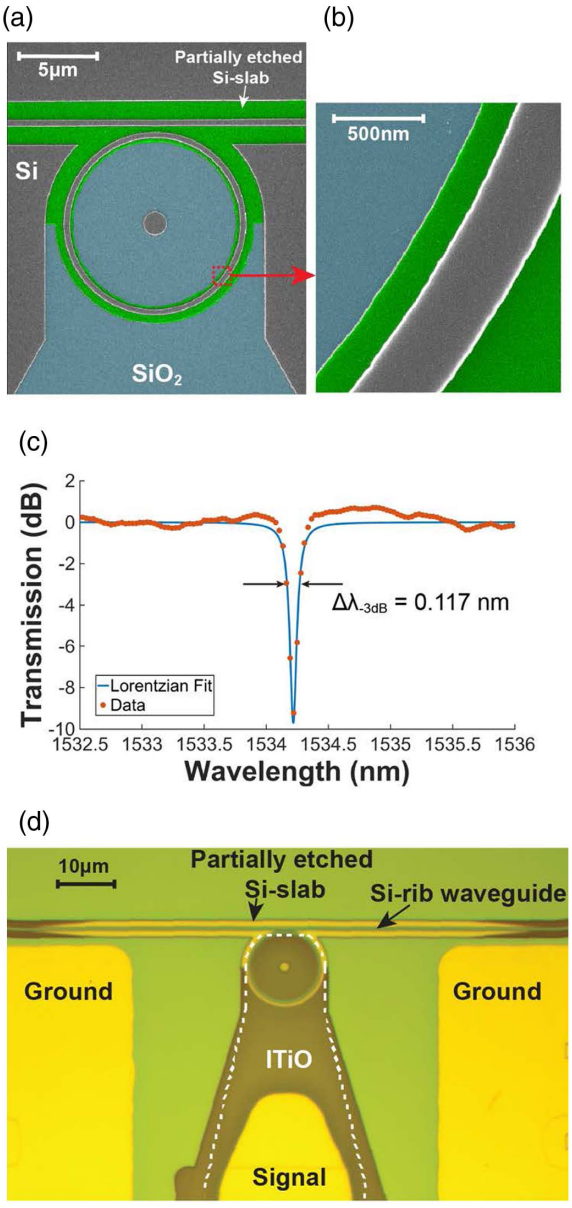

Fig. 3. (a) Scanning electron microscope (SEM) image of the fabricated passive Si-MRR with false colors. The microring has a radius of 6 μm. (b) Zoom-in SEM image of microring to show the side-wall roughness. (c) The experimental transmission spectrum of the passive MRR, which is fitted by the Lorentzian function, has a high Q factor of ~13,000. (d) Optical image of the fabricated ITiO-gated MOS MRR. The ITiO gate, which is highlighted by the white dashed line, covers the active region of the microring except the coupling region to the bus waveguide. The active region covers ~83% of the MRR. The gate electrode lies on ITiO, and the ground electrodes are connected to the p-Si microring through a partially etched Si slab.

patterned by two steps of electron beam lithography (EBL) and reactive ion etching (RIE), which has a 250 nm thick rib waveguide and a 50 nm thick slab. The MRRs have a radius of 6 μm, as shown in Figs. 3(a) and 3(b). Further, different gaps of MRRs are fabricated on the same SOI wafer to achieve the critical coupling condition. Figure 3(c) shows the experimental transmission spectrum of the passive MRR. The Q factor is obtained by the Lorentzian fitting to the experimental data, which is a widely adopted method to quantify high-Q resonators [33]. The Q factor is determined by $\lambda_{res}/\Delta\lambda_{-3\,dB}$. The passive MRR has a high Q factor of 13,000.

Next, a 17 nm thick SiO_2 layer is formed by dry oxidation at 1000°C, and a 17 nm ITiO gate is deposited by radio frequency (RF) sputtering at room temperature, followed by a lift-off photolithography process. The ITiO is characterized by Hall effect measurement, which has the N_c of 2.63×10^{19} cm^{-3} and μ_{bulk} of 26.5 $cm^2 \cdot V^{-1} \cdot s^{-1}$. The SiO_2 layer on the Si contact region is etched by hydrofluoric (HF) acid. Finally, the Ni/Au electrodes are thermally evaporated and patterned by regular photolithography. For characterization of the ITiO-gated MOS MRRs, the input and output fibers have a tilt angle of 8°, and the polarization controller is used to make the input light in the TE mode. The light is coupled into and out from the silicon bus waveguide through the waveguide grating couplers. The gate voltage is applied through the GSG electrodes from the GSG probe. Finally, the transmission spectra with different V_g are detected by an optical spectrum analyzer.

B. Experimental Results

In this work, the initial condition of ITiO is measured, which has the N_c of $(2.624 \pm 0.014) \times 10^{19}$ cm^{-3} and μ_{bulk} of 26.5 ± 0.15 $cm^2 \cdot V^{-1} \cdot s^{-1}$. Hence, we can build the experimental Q factor map with these parameters (N_c and μ_{bulk}), and this Q factor map can be used to derive the $\mu_{op,FE}$ with the experimental results.

Figure 4(a) shows the experimental spectra of the normalized transmission with different negative V_g. Experimental Q factors and $\Delta\lambda$ as a function of the V_g are plotted in Fig. 4(b), which shows that the $\Delta\lambda$ is linearly proportional to V_g when the V_g is beyond −2 V. It has an average wavelength tunability of 48.5 pm/V, and the Q factor is still higher than 4000 when it has a cumulative $\Delta\lambda$ of 500 pm. Next, we can derive the $\mu_{op,FE}$ by mapping the experimental $\Delta\lambda$ and Q factor to the simulation results. Figure 4(c) plots the extraction of the $\mu_{op,FE}$.

Since this method is an indirect method to estimate the $\mu_{op,FE}$, we need to discuss its accuracy. The major error sources come from the experimental results in Fig. 4(b) with the simulation in Fig. 1(c). For the wavelength tunability, the experiment (48.5 pm/V) matches the simulation (51.9 pm/V) with a standard deviation of 7%. For the Q factor, we can first compare it at the initial condition ($V_g = 0$ V) because it does not have any change of ΔN and $\mu_{op,FE}$ in the accumulation layer. Therefore, we can directly see the difference between experiment and simulation when we use the same parameters. The experiment matches very well with the simulation at $V_g = 0$ V, which only has an error of <1%. Even though the Q factor error increases when a larger gate bias is applied, it is still less than 5%. The error from the mismatch causes the error of $\mu_{op,FE}$ ($\Delta\mu_{op,FE}$), which is 2.5 $cm^2 \cdot V^{-1} \cdot s^{-1}$. The other source of errors comes from the experiment measurement. The experimentally measured Q factors are $Q \pm 50$. This standard deviation can cause a $\Delta\mu_{op,FE}$ of ~3 $cm^2 \cdot V^{-1} \cdot s^{-1}$. However, in the small V_g region, it can even be as large as $\Delta\mu_{op,FE}$ of $5 - 10$ $cm^2 \cdot V^{-1} \cdot s^{-1}$ due to the small relative change. In addition, the λ_{res} may have ±2 pm difference during the

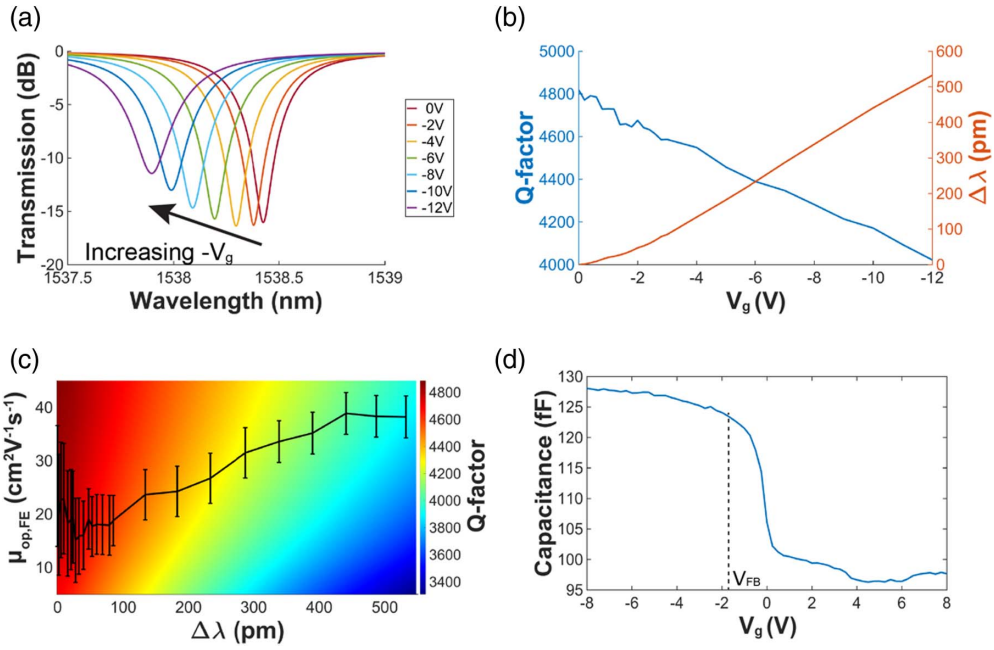

Fig. 4. (a) Lorentzian fitted experimental transmission spectra of ITiO-gated MOS MRR with different V_g. (b) Experimental Q factor (blue line, left y axis) and $\Delta\lambda$ (red line, right y axis). (c) $\mu_{op,FE}$ extraction from experimental Q factor and $\Delta\lambda$ with errors. (d) Capacitance as a function of V_g for the ITiO-gated MOS MRR.

measurement, which induces $\Delta\mu_{FE}$ of 1 $cm^2 \cdot V^{-1} \cdot s^{-1}$. The measurement errors from N_c and μ_{bulk} are minor and cause $\Delta\mu_{op,FE}$ of 0.7 and 1 $cm^2 \cdot V^{-1} \cdot s^{-1}$, respectively. The overall error of $\Delta\mu_{op,FE}$ is combined with

$$\Delta\mu_{op,FE(all)} = \sqrt{\Delta\mu^2_{op,FE(mismatch)} + \Delta\mu^2_{op,FE(Q)} + \Delta\mu^2_{op,FE(\Delta\lambda)} + \Delta\mu^2_{op,FE(Nc)} + \Delta\mu^2_{op,FE(\mu bulk)}}.$$

Finally, the error bars are plotted in Fig. 4(c) together with the mobility results. Figure 4(c) results show that the $\mu_{op,FE}$ has a large fluctuation in the small V_g region (0 to −2 V). We can determine the accumulation mode region ($V_g < -2$ V) from Fig. 4(b) since the $\Delta\lambda$ is linearly proportional to V_g in the accumulation mode [39]. The flat band voltage (V_{FB}) is also found to be around −2 V from the capacitance–voltage curve of the device, as shown in Fig. 4(d). This method can only achieve meaningful results when the field-effect is obvious. When the V_g is small (0 to −2 V), the change of the carrier concentration is relatively minor compared to the bulk concentration. Therefore, the change of the Q factor and $\Delta\lambda$ are difficult to measure accurately, which induces a large fluctuation when V_g is low. In the obvious accumulation mode region ($V_g < -2$ V), when the ΔN becomes larger, the measurement error does not have a significant influence. Hence, we can see that the $\mu_{op,FE}$ increases steadily in the moderate to strong accumulation mode. It shows a trend of increasing $\mu_{op,FE}$ from 25.3 to 38.4 $cm^2 \cdot V^{-1} \cdot s^{-1}$ as the negative V_g increases. Interestingly, a similar phenomenon is also mentioned in the TFT measurement when measuring the electric frequency μ_{FE}, and it shows a stable growth of electric frequency μ_{FE} in accumulation mode but not in the depletion mode [40,41]. When the larger negative V_g is applied, it has a higher $\mu_{op,FE}$ in the accumulation layer, reducing the optical absorption loss. Therefore, it can help the ITiO-gated MOS MRR maintain a good Q factor even though a larger negative V_g is applied.

4. CONCLUSION

In conclusion, we invented a new characterization method for quantifying the $\mu_{op,FE}$ in the accumulation channel by a tunable ITiO-SiO_2-Si MOS-driven MRR. The proposed integrated photonic platform provides dramatically stronger light–matter interaction compared with the traditional ellipsometry measurement. By constructing a comprehensive numerical model, we generated the contour map of the Q factor of the MRR with respect to $\mu_{op,FE}$ and $\Delta\lambda$ by sweeping ΔN and $\mu_{op,FE}$ in the simulation. Experimental results of the Q factor and $\Delta\lambda$ were measured under the negative V_g and subsequently used to derive the $\mu_{op,FE}$ by mapping the data into the simulation results. Our experimental results demonstrated that the $\mu_{op,FE}$ of ITiO increases from 25.3 to 38.4 $cm^2 \cdot V^{-1} \cdot s^{-1}$ with increasing V_g, which shows a similar trend in the electric frequency μ_{FE}. This method provides a novel pathway to precisely obtain the in-device $\mu_{op,FE}$ from an integrated photonics platform that has never been explored. Our approach fills the gap of existing carrier mobility characterization methods for field-effect electro-optic devices, especially for heterogeneously integrated silicon photonic devices.

Funding. National Aeronautics and Space Administration (80NSSC21K0230); National Science Foundation Directorate for Engineering (1927271); Air Force Office of Scientific Research (FA9550-17-1-0071).

Acknowledgment. The authors would like to acknowledge the Oregon State University Materials Synthesis and Characterization Facility (MASC) and Electronic Microscopy Facility for their support in device fabrication, and Prof. Janet Tate at the Department of Physics for the Hall measurement.

Disclosures. The authors declare no conflicts of interest.

REFERENCES

1. C. T. Sah, "Evolution of the MOS transistor-from conception to VLSI," Proc. IEEE **76**, 1280–1326 (1988).
2. H. C. Lin, W. E. Wang, G. Brammertz, M. Meuris, and M. Heyns, "Electrical study of sulfur passivated $In_{0.53}Ga_{0.47}As$ MOS capacitor and transistor with ALD Al_2O_3 as gate insulator," Microelectron. Eng. **86**, 1554–1557 (2009).
3. M. K. Kim and J. S. Lee, "Synergistic improvement of long-term plasticity in photonic synapses using ferroelectric polarization in hafnia-based oxide-semiconductor transistors," Adv. Mater. **32**, 1907826 (2020).
4. A. Liu, R. Jones, L. Liao, D. Samara-Rubio, D. Rubin, O. Cohen, R. Nicolaescu, and M. Paniccia, "A high-speed silicon optical modulator based on a metal-oxide-semiconductor capacitor," Nature **427**, 615–618 (2004).
5. W. Cai, J. S. White, and M. L. Brongersma, "Power-efficient electrooptic plasmonic modulators," Nano Lett. **9**, 4403–4411 (2009).
6. K. Debnath, D. J. Thomson, W. Zhang, A. Z. Khokhar, C. Littlejohns, J. Byers, L. Mastronardi, M. K. Husain, K. Ibukuro, F. Y. Gardes, G. T. Reed, and S. Saito, "All-silicon carrier accumulation modulator based on a lateral metal-oxide-semiconductor capacitor," Photon. Res. **6**, 373–379 (2018).
7. M. Midrio, P. Galli, M. Romagnoli, L. C. Kimerling, and J. Michel, "Graphene-based optical phase modulation of waveguide transverse electric modes," Photon. Res. **2**, A34–A40 (2014).
8. J. H. Han, F. Boeuf, J. Fujikata, S. Takahashi, S. Takagi, and M. Takenaka, "Efficient low-loss InGaAsP/Si hybrid MOS optical modulator," Nat. Photonics **11**, 486–490 (2017).
9. R. Amin, R. Maiti, C. Carfano, Z. Ma, M. H. Tahersima, Y. Lilach, D. Ratnayake, H. Dalir, and V. J. Sorger, "0.52 V mm ITO-based Mach-Zehnder modulator in silicon photonics," APL Photon. **3**, 126104 (2018).
10. E. Feigenbaum, K. Diest, and H. A. Atwater, "Unity-order index change in transparent conducting oxides at visible frequencies," Nano Lett. **10**, 2111–2116 (2010).
11. Q. Gao, E. Li, and A. X. Wang, "Ultra-compact and broadband electroabsorption modulator using an epsilon-near-zero conductive oxide," Photon. Res. **6**, 277–281 (2018).

12. E. Li, Q. Gao, S. Liverman, and A. X. Wang, "One-volt silicon photonic crystal nanocavity modulator with indium oxide gate," Opt. Lett. **43**, 4429–4432 (2018).
13. E. Li, B. A. Nia, B. Zhou, and A. X. Wang, "Transparent conductive oxide-gated silicon microring with extreme resonance wavelength tunability," Photon. Res. **7**, 473–477 (2019).
14. S. H. Mir, V. K. Yadav, J. K. Singh, and J. K. Singh, "Recent advances in the carrier mobility of two-dimensional materials: a theoretical perspective," ACS Omega **5**, 14203–14211 (2020).
15. S. D'Elia, N. Scaramuzza, F. Ciuchi, C. Versace, G. Strangi, and R. Bartolino, "Ellipsometry investigation of the effects of annealing temperature on the optical properties of indium tin oxide thin films studied by Drude-Lorentz model," Appl. Surf. Sci. **255**, 7203–7211 (2009).
16. J. Ederth, A. Hultåker, G. A. Niklasson, P. Heszler, A. R. Van Doorn, M. J. Jongerius, D. Burgard, and C. G. Granqvist, "Thin porous indium tin oxide nanoparticle films: effects of annealing in vacuum and air," Appl. Phys. A **81**, 1363–1368 (2005).
17. S. Campione, M. G. Wood, D. K. Serkland, S. Parameswaran, J. Ihlefeld, T. S. Luk, J. R. Wendt, K. M. Geib, and G. A. Keeler, "Submicrometer epsilon-near-zero electroabsorption modulators enabled by high-mobility cadmium oxide," IEEE Photon. J. **9**, 2723299 (2017).
18. B. Zhou, E. Li, Y. Bo, and A. Wang, "High-speed plasmonic-silicon modulator driven by epsilon-near-zero conductive oxide," J. Lightwave Technol. **38**, 3338–3345 (2020).
19. T. I. Kamins, "Hall mobility in chemically deposited polycrystalline silicon," J. Appl. Phys. **42**, 4357–4365 (1971).
20. Y. Sago and H. Fujiwara, "Mapping characterization of SnO_2:F transparent conductive oxide layers by ellipsometry technique," Jpn. J. Appl. Phys. **51**, 10NB01 (2012).
21. Z. Ma, Z. Li, K. Liu, C. Ye, and V. J. Sorger, "Indium-tin-oxide for high-performance electro-optic modulation," Nanophotonics **4**, 198–213 (2015).
22. K. I. Goto, T. H. Yu, J. Wu, C. H. Diaz, and J. P. Colinge, "Mobility and screening effect in heavily doped accumulation-mode metal-oxide-semiconductor field-effect transistors," Appl. Phys. Lett. **101**, 073503 (2012).
23. J. F. Wager, D. A. Keszler, and R. E. Presley, *Transparent Electronics* (Springer, 2008).
24. R. L. Huffman, "ZnO-channel thin-film transistors: channel mobility," J. Appl. Phys. **95**, 5813–5819 (2004).
25. Y. Nitzan, M. Grinshpan, and Y. Goldstein, "Field-effect mobility in quantized accumulation layers on ZnO surfaces," Phys. Rev. B **19**, 4107–4115 (1979).
26. C. J. Chiu, S. P. Chang, and S. J. Chang, "Transistor using Ta_2O_5 gate dielectric," IEEE Electron Device Lett. **31**, 1245–1247 (2010).
27. Y. Chen, D. Geng, M. Mativenga, H. Nam, and J. Jang, "High-speed pseudo-CMOS circuits using bulk accumulation a-IGZO TFTs," IEEE Electron Device Lett. **36**, 153–155 (2015).
28. Y. Shin, S. T. Kim, K. Kim, M. Y. Kim, S. Oh, and J. K. Jeong, "The mobility enhancement of indium gallium zinc oxide transistors via low-temperature crystallization using a tantalum catalytic layer," Sci. Rep. **7**, 10885 (2017).
29. J. Steinhauser, S. Faÿ, N. Oliveira, E. Vallat-Sauvain, and C. Ballif, "Transition between grain boundary and intragrain scattering transport mechanisms in boron-doped zinc oxide thin films," Appl. Phys. Lett. **90**, 142107 (2007).
30. H. C. M. Knoops, B. W. H. van de Loo, S. Smit, M. V. Ponomarev, J.-W. Weber, K. Sharma, W. M. M. Kessels, and M. Creatore, "Optical modeling of plasma-deposited ZnO films: electron scattering at different length scales," J. Vac. Sci. Technol. A **33**, 021509 (2015).
31. H. Fujiwara and M. Kondo, "Effects of carrier concentration on the dielectric function of ZnO:Ga and In_2O_3:Sn studied by spectroscopic ellipsometry: analysis of free-carrier and band-edge absorption," Phys. Rev. B **71**, 075109 (2005).
32. G. V. Naik, V. M. Shalaev, and A. Boltasseva, "Alternative plasmonic materials: beyond gold and silver," Adv. Mater. **25**, 3264–3294 (2013).
33. W. Bogaerts, P. de Heyn, T. van Vaerenbergh, K. de Vos, S. Kumar Selvaraja, T. Claes, P. Dumon, P. Bienstman, D. van Thourhout, and R. Baets, "Silicon microring resonators," Laser Photon. Rev. **6**, 47–73 (2012).
34. W. Shi, X. Wang, W. Zhang, H. Yun, C. Lin, L. Chrostowski, and N. A. F. Jaeger, "Grating-coupled silicon microring resonators," Appl. Phys. Lett. **100**, 121118 (2012).
35. J. Xie, L. Zhou, X. Sun, Z. Zou, L. Lu, H. Zhu, X. Li, and J. Chen, "Selective excitation of microring resonances using a pulley-coupling structure," Appl. Opt. **53**, 878–884 (2014).
36. I. Demirtzioglou, C. Lacava, K. R. H. Bottrill, D. J. Thomson, G. T. Reed, D. J. Richardson, and P. Petropoulos, "Frequency comb generation in a silicon ring resonator modulator," Opt. Express **26**, 790–796 (2018).
37. X. Cheng, J. Hong, A. M. Spring, and S. Yokoyama, "Fabrication of a high-Q factor ring resonator using LSCVD deposited Si_3N_4 film," Opt. Mater. Express **7**, 2182–2187 (2017).
38. Q. Gao, E. Li, and A. X. Wang, "Comparative analysis of transparent conductive oxide electro-absorption modulators [Invited]," Opt. Mater. Express **8**, 2850–2862 (2018).
39. E. Li, Q. Gao, R. T. Chen, and A. X. Wang, "Ultracompact silicon-conductive oxide nanocavity modulator with 0.02 lambda-cubic active volume," Nano Lett. **18**, 1075–1081 (2018).
40. A. Zeumault and V. Subramanian, "Improved technique for quantifying the bias-dependent mobility of metal-oxide thin-film transistors," IEEE Trans. Electron Devices **62**, 855–861 (2015).
41. A. Zeumault and V. Subramanian, "Mobility enhancement in solution-processed transparent conductive oxide TFTs due to electron donation from traps in high-*k* gate dielectrics," Adv. Funct. Mater. **26**, 955–963 (2016).